

# Multilayer Nanoporous Graphene Membranes for Water Desalination

David Cohen-Tanugi,<sup>†</sup> Li-Chiang Lin,<sup>†,‡</sup> and Jeffrey C. Grossman\*,<sup>†</sup>

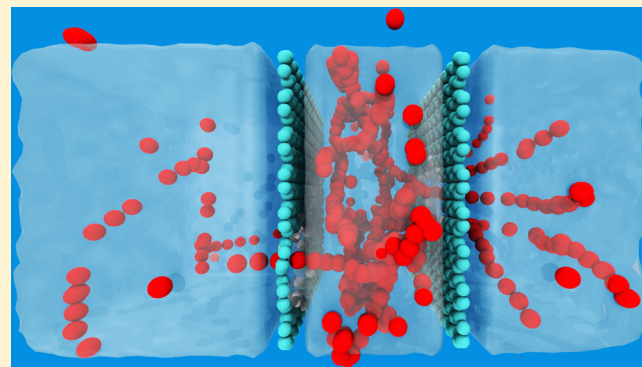
<sup>†</sup>Department of Materials Science and Engineering, Massachusetts Institute of Technology, Cambridge, Massachusetts 02139, United States

<sup>‡</sup>Department of Process and Energy, Delft University of Technology, Delft, 2628 CB, The Netherlands

## Supporting Information

**ABSTRACT:** While single-layer nanoporous graphene (NPG) has shown promise as a reverse osmosis (RO) desalination membrane, multilayer graphene membranes can be synthesized more economically than the single-layer material. In this work, we build upon the knowledge gained to date toward single-layer graphene to explore how multilayer NPG might serve as a RO membrane in water desalination using classical molecular dynamic simulations. We show that, while multilayer NPG exhibits similarly promising desalination properties to single-layer membranes, their separation performance can be designed by manipulating various configurational variables in the multilayer case. This work establishes an atomic-level understanding of the effects of additional NPG layers, layer separation, and pore alignment on desalination performance, providing useful guidelines for the design of multilayer NPG membranes.

**KEYWORDS:** Water desalination, ultrathin-film membrane, multilayer nanoporous graphene, molecular dynamic simulation



Nanoporous graphene (NPG) membranes have drawn considerable attention for their potential in reverse osmosis (RO) desalination, which could lead to a more economical and energy-efficient RO process to separate salts from saline water.<sup>1–3</sup> Most studies to date have considered an idealized, single-layer system with variations in several key parameters (i.e., nanopore size, chemistry, or substrate morphology), with the aim of guiding the experimental synthesis of NPG membranes.<sup>2–4</sup>

Although multiple efforts have targeted the synthesis of large-scale graphene films,<sup>5</sup> producing perfect monolayer graphene over large areas remains highly challenging experimentally. In particular, the primary method that has been used to date for synthesizing graphene sheets, chemical vapor deposition, results in substantial multilayer coverage, in addition to Stone–Wales (5–7 ring) defects,<sup>6</sup> tears, and other intrinsic defects.<sup>7</sup> Thus, pristine, monolayer regions rarely exceed ~1 mm<sup>2</sup>.<sup>8</sup> Multilayer coverage can be expected to become even more relevant with the development of solution processing as a potentially cheap, scalable, and high-yield approach to graphene membrane production.<sup>9–11</sup> However, because this approach involves assembling a planar sheet from even smaller, micrometer-sized graphene flakes, solution-processed graphene membranes will include multiple layers stacked on top of each other. While several studies indicate that it may be possible to “stitch” the graphene flakes together,<sup>12–14</sup> the resulting sheet will nevertheless likely consist of multiple layers.

At present, the physical implications of these multiple graphene layers on the membrane’s performance are largely

unknown. In particular, it is unclear whether NPG will maintain its water permeability if the material no longer consists of a single atomic layer. Moreover, it is unknown how the interplay between nanopores on different layers would influence the membrane’s water permeation and salt rejection ability. These questions are critical to the technical viability of graphene membranes, and it is therefore essential to understand how multilayer NPG performs as an RO membrane. In this work, we carry out classical molecular dynamics (MD) simulations to investigate the effects of layering on RO performance, taking a bilayer NPG membrane as a model system. An underlying assumption is that the transition from a single layer to two layers will teach us the most important effects of adding layers to an NPG membrane and that subsequent layers will have a qualitatively similar effect. We note that a better understanding of the implications of multilayer NPG membranes would be also of direct relevance to recently developed stacking graphene oxide (GO) membranes<sup>15,16</sup> as well as many other classes of ultrathin-film membrane candidates such as graphyne,<sup>17–19</sup> covalent triazine frameworks,<sup>20</sup> nanoporous reduced GO,<sup>21</sup> and MoS<sub>2</sub>.<sup>22</sup>

MD simulations are ideally suited to study this system because they allow us to probe the kinetics and thermodynamics of desalination while accounting for the physics of

**Received:** October 8, 2015

**Revised:** January 12, 2016



ACS Publications

© XXXX American Chemical Society

A

DOI: 10.1021/acs.nanolett.5b04089  
Nano Lett. XXXX, XXX, XXX–XXX

water, ions, and graphene layers with high accuracy. MD simulations compute the evolution of a system of atoms from an original configuration and under a set of constraints.<sup>23</sup> These simulations work by calculating the forces between atoms at each time step, and updating the positions of all the atoms at the following time step using Newton's equations of motion. Depending on the choice of force field, the behavior of relatively large molecular systems ( $10^2$ – $10^9$  atoms) can be investigated over physically meaningful time scales (typically between 1 ns and 1  $\mu$ s).

The studied system consisted of a membrane (made of bilayer graphene) with saline feedwater (with an NaCl concentration of 0.5 M) on one side and pure permeate water on the other, and bounded by rigid pistons designed to apply a transmembrane pressure. We studied the RO performance of bilayer NPG across a wide range of configurational parameters. For each nanopore radius  $R$ , we examined the effects of the different parameters on the properties of the membrane. The key parameters that we explored were the feed pressure  $P$ , the offset  $O$  between nanopores in the upstream and downstream graphene layer, and the spacing  $H$  between graphene layers (see Figure 1).

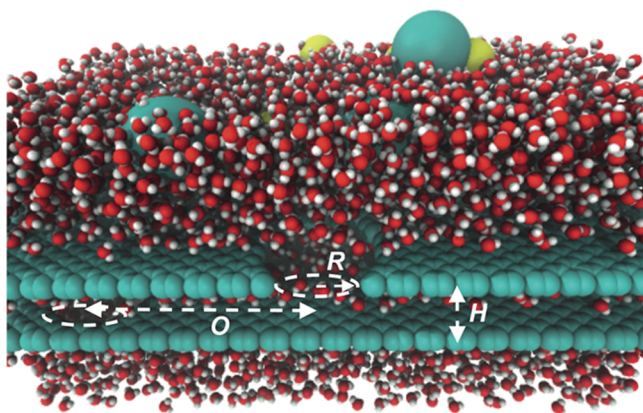


**Figure 1.** Bilayer membrane with nanopore radius  $R$ , layer separation  $H$ , and nanopore offset  $O$ .

The interlayer spacing can be as narrow as  $H = 3.35$  Å (which corresponds to the layer spacing found in graphite), or can in principle be much greater, e.g., if rigid nanoparticles were evenly intercalated between the graphene sheets. In order to explore a regime in which the layer separation is larger than the characteristic pore size, we chose a maximum layer separation of  $H = 20$  Å. Furthermore, these spacings are physically relevant because separations of 10 and 14 Å yield two and three water layers, respectively.<sup>24</sup> The pore offset varied from  $O = 0$  Å (fully aligned pores) to 19.6 Å, which corresponds to maximally offset pores given the size of our unit cell. We note that larger unit cells would allow for larger pore offsets (in addition to lower pore densities).

The system geometries were built using VMD 1.9.1<sup>25</sup> and Avogadro 1.1.1.<sup>26</sup> The initial distance between the feed piston and the upstream membrane was set to 5 nm in order to remove size effects in the feed. The distance between the permeate piston and the downstream membrane was initially set to 2 nm, and is expected to increase over the course of the simulation as feedwater molecules move to the permeate side. The cross-section of the unit cell was approximately 3 nm by 3 nm. The interlayer region was initially hydrated with pure

water. Nanopores were created by removing carbon atoms within 4 and 6 Å from the center of a hexagonal graphene ring. By representing atoms as vdW spheres, we calculated the radius ( $R$ ) of these nanopores to be approximately 3.0 and 4.5 Å, respectively (see Figure 1). The nanopore edges were then functionalized with hydrogen groups using Avogadro. The nanopores in neighboring graphene layers were offset diagonally from each other in increments corresponding to the separation between consecutive hexagonal rings in graphene ( $\delta x = 1.228$  Å,  $\delta y = 2.127$  Å). Thus, the offset between two nanopores that are one unit away from each other was  $(\delta x^2 + \delta y^2)^{1/2} = 2.456$  Å.

MD simulations were carried out using the LAMMPS package<sup>27</sup> to predict the desalination performance of bilayer NPG with different system parameters. To obtain meaningful statistics, for each set of parameters more than 8 independent simulations were performed. In all simulations, to substantially reduce the computational cost, we assumed all the membrane atoms were held rigid. The deformation effect of NPG membranes on desalination performance (i.e., permeability) under a high hydraulic pressure was found to be marginal.<sup>28</sup> To describe intermolecular interactions (i.e., salt water–salt water and salt water–membrane), a Lennard–Jones (LJ) plus Coulomb potential was used. We used the TIP4P-Ew<sup>29</sup> model for water molecules and the corresponding parameters proposed by Joung et al. for  $\text{Na}^+$  ions and for  $\text{Cl}^-$  ions.<sup>30</sup> For graphene, the LJ parameters of carbon atoms away from the pore edges were adopted from the work of Beu et al.,<sup>31</sup> while the LJ parameters and atomic charges for the hydrogenated groups were taken from the study of Mooney et al.<sup>32</sup> For all pairwise LJ terms, the Lorentz–Berthelot mixing rules were applied. The simulations were performed in the NVT ensemble at 300 K using a Nosé–Hoover thermostat with a damping factor of 100 time steps, i.e., 100 fs. The adopted time step, 1 fs, was found to be sufficiently small to ensure energy conservation.

In each simulation, we tracked number of water molecules and salt ions in the feed, interlayer, and permeate regions over time. A typical simulation outcome of the number of water molecules over time is shown in Figure 2. The number of water molecules in the interlayer remained approximately constant, while the number of feed waters decreased at a constant rate and the number of permeate waters increased at the same rate. Although it is known that salt concentration affects the self-diffusivity of water molecules, the fact that water flow rate remains constant over time indicates that the effect of salt concentration on flow rate is small in the conditions studied here.

In order to estimate salt passage and water flow rate, a reference time is needed. For each simulation, we defined a time  $t_f$  that is representative of the end of the simulation. Because the water flow rate varied widely depending on nanopore size, we chose to define  $t_f$  as the time when 20% of the feedwater has permeated through the bilayer membrane (i.e., denoted as  $t_{1/5}$ ) in the case of  $R = 3.0$  Å, and when 50% of the feedwater has permeated (i.e., denoted as  $t_{1/2}$ ) in the case of  $R = 4.5$  Å. We chose this definition because it corresponds to approximately 20 ns of simulation time for both nanopore sizes. This choice of definition for  $t_f$  means that it is more difficult to compare the salt rejection across different pore sizes, but it has the distinct advantage of allowing us to maximize the amount of data available for each system as well as reduce the required computation time for systems with smaller pore sizes. In this

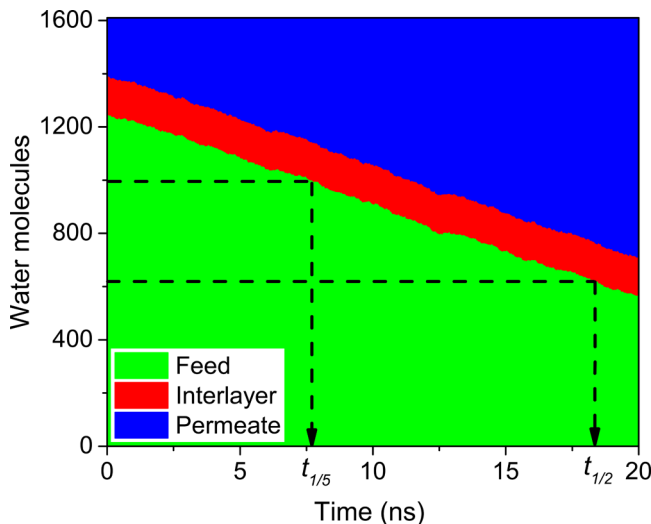


**Figure 2.** Number of water molecules in the feed (green), interlayer (red), and permeate region (blue) as a function of simulation time for a typical simulation. The  $t_{1/5}$  and  $t_{1/2}$  for this particular simulation are highlighted.

study, the relative number of salt ions that passed into the permeate region during the simulation was used to estimate salt rejection ( $R$ ) for each membrane. Salt rejection is defined as  $R = (N_f^0 - N_p)/N_f^0$ , where  $N_p$  is the number of salt ions (i.e., average number of  $\text{Na}^+$  and  $\text{Cl}^-$  ions) in the permeate at  $t = t_f$ , while  $N_f^0$  is the initial number of salt ions in the feed at  $t = 0$ . The water flow rate per pore was determined by the slope of the number of water molecules that permeated through the membrane from  $t_0$  to  $t_f$ . Our MD system can be characterized as a dead-end filtration system, insofar as the feed reservoir is finite. While dead-end filtration studies are a common way to investigate the steady-state properties of a membrane both experimentally and computationally, proper care must be taken when estimating salt rejection. Here, the observed salt rejection can only be extrapolated to steady-state for those systems in which the amount of water that enters the permeate region is significantly larger than the amount of pure water that was initially in the interlayer region.

We note here that the pressures employed in our simulations are significantly greater than the pressures applied in RO plants (<8 MPa). High simulated pressures on the order of ~100 MPa allow us to obtain more precise data for water flux and salt rejection given a finite simulation time (i.e., order of 10 ns). This approach is justified by the fact that water flux scales linearly with net driving pressure, meaning that results obtained at hundreds of MPa can be extrapolated to calculate the water flux that would result from lower net driving pressures in an RO system.<sup>28</sup>

Overall, our results indicate that a bilayer NPG membrane could act as an effective RO membrane. We also observe several trends that indicate how the relative placement of the NPG layers can affect the membrane properties, resulting in useful guidelines for the design of multilayer NPG membranes.

**Water Flow Rate.** We have investigated the effects of pressure, bilayer separation, and nanopore offset on water flow rate in detail. The results are shown in Figures 3a–c. Figure 3a shows how water flow rate per pore evolves with the applied pressure for the case of  $H = 8 \text{ \AA}$  and  $O = 0 \text{ \AA}$ , under the assumption that the interlayer spacing remains fixed. The figure indicates that the flow rate for a given bilayer system scales

linearly with the applied pressure. This relationship is consistent with recent work for single-layer NPG membranes<sup>3,28</sup> and with classical membrane theory.<sup>33</sup> An experimental multilayer membrane may potentially experience compacting upon the application of pressure, which would result in smaller interlayer spacing. The extent to which compacting occurs will depend on the nature of the structure keeping the layers separate from each other (e.g., rigid nanoparticles, nanorods, flexible spacers). The effect of different spacers lies beyond the scope of this study.

Next, we turn to the effect of layer spacing on water flow rate. Figure 3b shows the evolution of water flow rate with bilayer separation for two different pore alignments and  $\Delta P = \sim 100 \text{ MPa}$ . We observe that when the layers are sufficiently spaced ( $H \geq 8 \text{ \AA}$ ), the water flow rate is independent of layer spacing. This continues to hold at very large layer separations ( $H = 30 \text{ \AA}$ , see SI Figure S1) and suggests that water flow rate is governed by the energy barriers of the separate layers. To understand this finding, we have computed the free energy profiles of water as a function of layer separation (see Figure 4a and SI Figure S2). The free energy profiles are computed along the Z-direction (i.e., perpendicular to the membrane), as  $G(z) = -k_B T \ln(\rho(z))$ . Figure 4a indicates that the free energy profiles of water in a bilayer membrane with a large separation consist of two barriers for transport, and each of them is identical to the barrier of a single-layer membrane. This does not mean that no effects exist between the layers: indeed, we will see below that pore alignment can still affect the average time for a water molecule to cross the interlayer. But as far as water flow rate is concerned, the two graphene sheets act as resistors in series in a resistance-in-series model, and the resistance between two layers is negligible. Quantitatively, the water flow rate per pore for  $H \geq 8 \text{ \AA}$  equals approximately 50% of the flow rate across a single layer, which is consistent with the resistance-in-series model.

For an  $N$ -layer membrane, the total hydraulic resistance across the membrane would equal the sum of the resistances of the individual layer as long as the separation between consecutive layers is sufficiently large ( $H \geq 8 \text{ \AA}$ ). Its resulting flow rate  $\Phi_T$  thus follows:

$$\Phi_T = \left( \sum_{i=1}^N 1/\Phi_i \right)^{-1}$$

Multilayer membranes may possess varying pore sizes in different layers. Therefore, we also investigated an inhomogeneous bilayer system in which the upstream layer has pores of  $R = 3.0 \text{ \AA}$  and the downstream layer has pores of  $R = 4.5 \text{ \AA}$ , with a separation of  $14 \text{ \AA}$  and an offset of  $0 \text{ \AA}$  at approximately 100 MPa. This system yields a water flow rate of ~17 waters/ns/pore, which is consistent with the resistance predicted for these two membranes connected in series:

$$\Phi_T = (1/\Phi_{R3.0} + 1/\Phi_{R4.5})^{-1} \approx 17 \text{ waters/pore/ns}$$

Figure 3b also indicates that the cases of fully offset and fully aligned pores have comparable water flow rate, as long as  $H$  is large enough ( $\geq 8 \text{ \AA}$ ). To investigate the effect of pore offset on water flow rate in greater detail, Figure 3c shows the flow rate per pore as a function of pore offset. As shown in Figure 3c, the water flow rate is nearly independent of the pore offset although a small but still notable variation can be seen for bilayer NPG membranes with a larger pore size (i.e.,  $R = 4.5 \text{ \AA}$ ). Interestingly, this small variation is found to directly reflect on

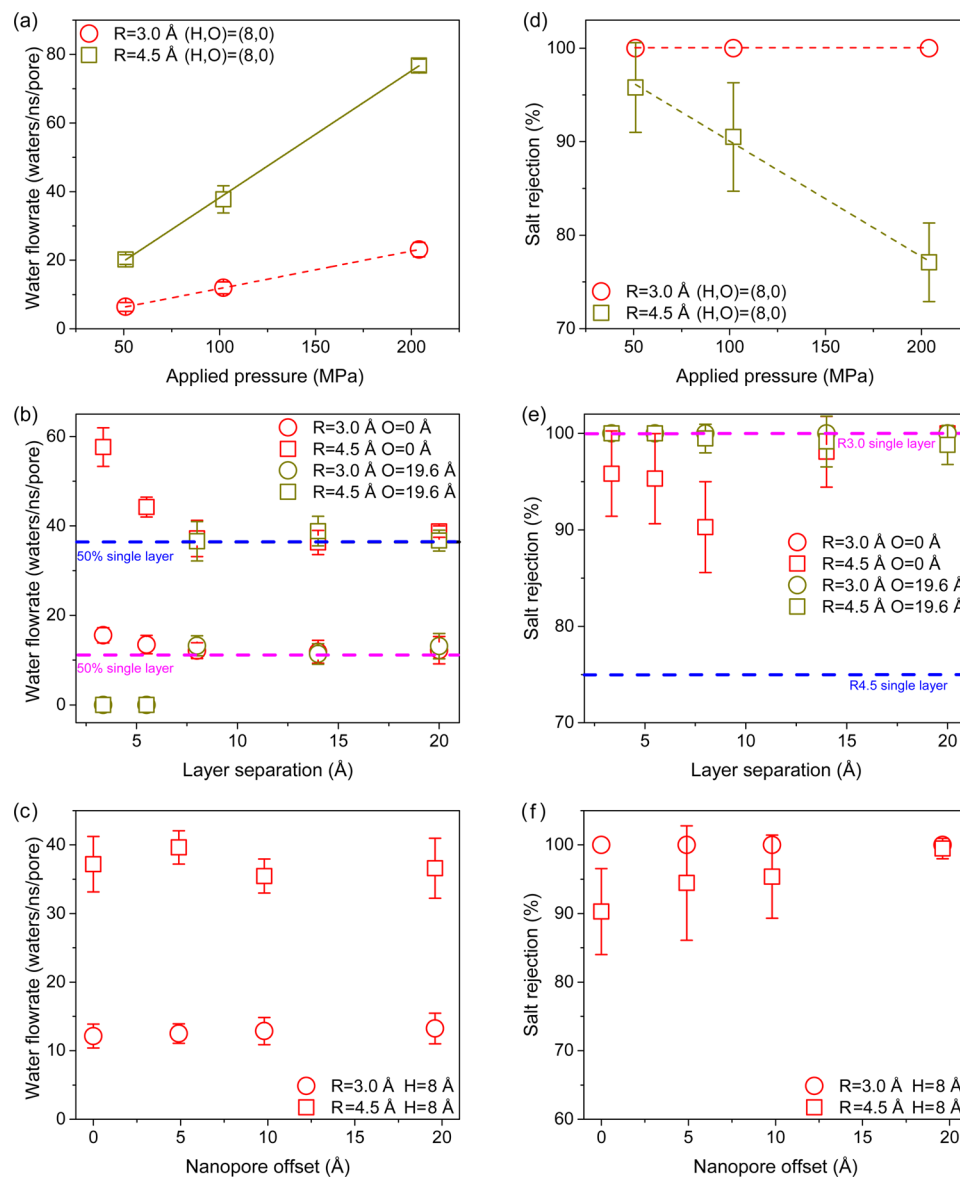


**Figure 3.** Effects of membrane configurational parameters on the water flow rate per pore (a–c) and salt rejection (d–f) of bilayer membranes: (a,d) effects of pressure, (b,e) effects of layer separation at different pore offsets (i.e.,  $O = 0 \text{ \AA}$  and  $O = 19.6 \text{ \AA}$ ), and (c,f) effects of pore offset at a layer separation of  $8 \text{ \AA}$ .

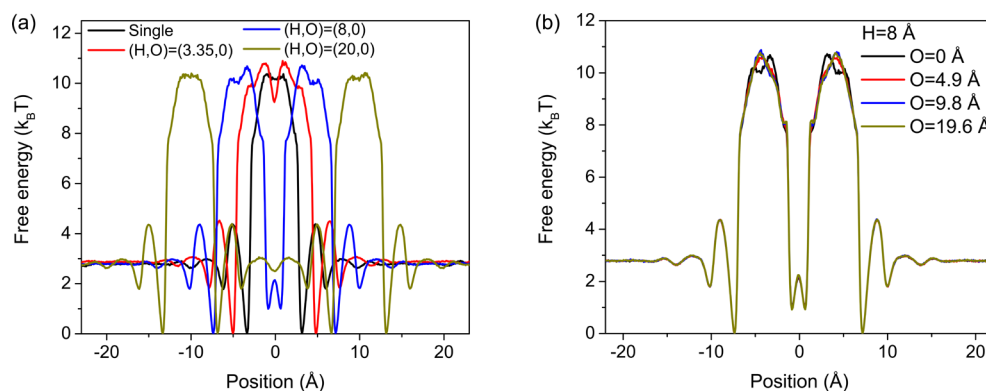


**Figure 4.** Water free energy profiles of bilayer NPG membranes as a function of (a) layer separation and (b) pore offset. For (a), systems at a constant pore offset of  $0 \text{ \AA}$  are studied, while for (b), systems at a constant layer separation of  $8 \text{ \AA}$  are studied.

the free energy profiles as shown in Figure 4b. The interplay between the locations of pores on different layers can lead to

different molecular configurations (e.g., the difference in location of barrier peaks between the cases of  $O = 0 \text{ \AA}$  and

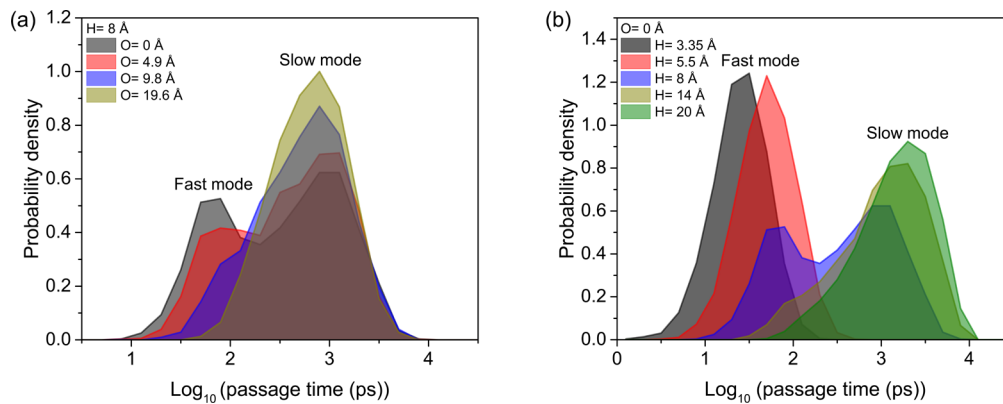


**Figure 5.** Probability density of the water permeation time for bilayer NPG with  $R = 4.5 \text{ \AA}$  for (a) different nanopore offsets at a constant layer separation of  $8 \text{ \AA}$  and (b) different layer separations at a constant pore offset of  $0 \text{ \AA}$ . The figure reveals a faster transport mode on the order of  $10 \text{ ps}$  (for bilayer membranes with aligned nanopores and small separations) that gradually disappears for membranes with misaligned pores and large separations.

$O = 4.9 \text{ \AA}$ ), resulting in marginal differences in transport barriers.

Furthermore, Figure 3b highlights a critical regime at  $H < 8 \text{ \AA}$ , in which water flow rate largely depends on pore offset as well as layer separation. As a result, the simple resistance-in-series model cannot be directly used to predict water flow rate for  $H < 8 \text{ \AA}$ . For completely aligned pores, the flow rate lies in between that of a single layer and that of two independent layers (i.e., it decays nonlinearly with increasing layer separation). A detailed inspection of the free energy barrier (Figure 4a) reveals that a small separation results in a system possessing a single barrier for transport, with the barrier height larger than a single-layer NPG membrane partially due to the stronger surface adsorption of water on the bilayer NPG surface. A transition from a small separation (single barrier with larger height) to a sufficiently large separation (two independent barriers) results in a nonlinear decay in flow rate. On the other hand, for maximally offset pores, the interspace region does not allow any water passage (i.e., zero flow rate) for both pore sizes. We have also investigated the effect of pore offset on water flow rate in this critical regime (i.e.,  $H < 8 \text{ \AA}$ ). SI Figure S3 shows that the water flow rate decreases when the nanopore offset becomes larger, which clearly suggests that a larger offset imposes a higher transport barrier for water. In addition, a smaller separation leads to a faster decrease in water flow rate as a function of increasing pore offset.

To further understand the nature of water flow through a bilayer NPG membrane, we computed the time it takes on average for a water molecule to permeate across the bilayer membrane, defined as the time spent in the interlayer region, from crossing the upstream membrane to leaving the downstream membrane. Figure 5a shows that the probability density of water passage times features two separate peaks in the case of aligned nanopores at  $H = 8 \text{ \AA}$ : a faster mode on the order of  $10 \text{ ps}$ , and a slower mode closer to  $1000 \text{ ps}$ . The fast mode gradually disappears for larger pore offsets, meaning that water molecules stay longer in the interlayer region. It is noteworthy that although the passage times span 2 orders of magnitude, the water flow rate remains approximately constant regardless of pore offset. Although surprising, this phenomenon is consistent with the fact that the net flow rate is governed by the free energy barrier across each membrane and is independent of the amount of time that water molecules

spend in the interlayer region. Figure 5b shows how this distribution of passage times evolves with layer separation (for fully aligned pores). Only the fast mode is observed for the case of  $H \leq 5.5$ , while the fast mode gradually diminishes for  $H \geq 8$ . As regards permeability, a water flow rate of  $38 \text{ waters/ns/pore}$  at  $\sim 100 \text{ MPa}$  results in a water permeability of  $209 \text{ L}/(\text{m}^2 \cdot \text{h} \cdot \text{bar})$ , assuming a pore density of  $5 \times 10^{12} \text{ pores per cm}^2$  for consistency with experimental results.<sup>34</sup>

**Salt Rejection.** We find that the bilayer NPG membrane is capable of rejecting salt for sufficiently small nanopores. Figure 3d–f shows the salt rejection across the membrane as a function of applied pressure, layer separation, and pore offset. The key results of these figures can be summarized as follows: (1) The bilayer NPG membranes with  $R = 3.0 \text{ \AA}$  consistently exhibit full salt rejection, whereas the bilayer  $R = 4.5 \text{ \AA}$  ones generally show a salt rejection of  $85\text{--}100\%$  at an applied pressure of approximately  $100 \text{ MPa}$ ; (2) Salt rejection decreases for greater pore alignment, larger layer spacing, or higher pressure; (3) The bilayer  $R = 4.5 \text{ \AA}$  membrane has an improved ability to reject salt compared to a single-layer membrane regardless of pore alignment or layer separation.

Figure 3d suggests that a pore size of  $3.0 \text{ \AA}$  is sufficiently small to efficiently block salt from passage, leading to  $100\%$  salt rejection at a wide range of applied pressures (i.e., up to  $\sim 200 \text{ MPa}$ ). NPG membranes with  $R = 4.5 \text{ \AA}$ , on the other hand, allow the passage of salt ions and exhibit a lower salt rejection at higher applied pressure. Whether or not higher pressure translates to lower salt rejection for a given membrane system will depend on the specific morphology of the interlayer structure, and in particular on the extent to which the interlayer spacing is affected by applied pressure. In addition, we saw above that the layer separation has a strong effect on water flow rate when  $H$  is less than  $8 \text{ \AA}$ .

Figure 3e further indicates that pore offset and layer separation significantly influence the membrane's ability to reject salt. With fully aligned pores, salt rejection decreases for greater  $H$ , suggesting that a narrow interlayer creates a size exclusion barrier beyond the effect of the nanopores. This effect is even more pronounced for the case of fully offset pores, where narrow interlayer spacings essentially block all salt ions from crossing at a separation less than  $8 \text{ \AA}$ , although water flow rate is also zero in these membrane configurations due to small separations. The observed salt rejection in the finite systems studied here can be accurately extrapolated to steady state for  $H$

= 3.35, 5.5, and 8 Å. For larger separations, the amount of pure water initially placed in the interlayer region approaches the same order as the total amount of fresh water that permeates across the membrane by the end of the simulation. In this regime, the salt rejection observed here cannot readily be extrapolated to steady state, and further studies will be needed. We note that in the limit of large  $H$ , it is expected that the two layers will act as independent membranes, meaning that the salt rejection of the multilayer system will have no further dependence on separation.

Finally, we have also investigated in detail the effect of pore offset by studying bilayer systems at  $H = 8$  Å and different offsets. Figure 3f indicates that similar to the results for small layer separations, pore offset plays an active role in improving salt rejection when  $H = 8$  Å. The narrow dimensions of the interlayer region may act as an energetic barrier to ions, with shorter pore–pore distances (i.e., aligned nanopores) allowing for a smaller transport barrier than large pore–pore distances (i.e., misaligned nanopores). This suggests a novel approach toward optimizing multilayer RO membranes, in which the offset between pores can be purposely maximized in order to increase salt rejection while maintaining a roughly constant water flow rate per pore. However, this approach would also result in lower pore density and lower net water flux (per membrane area). For instance, comparing the cases of  $O = 19.6$  Å and  $O = 4.9$  Å at  $H = 8$  Å, the theoretical pore density for the former case is 16 times lower, leading to a 16 times lower water flux per membrane area.

The aim of the results above is to assess the potential and the design of multilayer NPG membranes. We have found that parallel bilayer NPG layers at a large separation (i.e.,  $H \geq 8$  Å) act as a series of independent barriers for water, resulting in a flux penalty of 2× compared to single-layer membranes. For  $N$ -layer membranes at  $H \geq 8$  Å, the permeability can therefore be predicted using a resistance-in-series model. Similarly, increasing the number of layers results in greater salt rejection due to a higher diffusion resistance for ions. Although an NPG membrane's permeability will drop linearly as the number of graphene layers increases, the resulting permeability loss may represent an acceptable trade-off. Indeed, a membrane with 3× higher permeability than current commercial membranes would exhibit most of the energy efficiency and cost reduction improvements to be gained from more permeable membranes.<sup>1</sup>

Our results also provide guidelines for the design of multilayer membranes. We have found a critical region for membrane design at a layer separation of  $H \leq 8$  Å, in which layer separation and pore alignment both play a crucial role in determining desalination performance. Our simulations reveal that a smaller layer separation with fully aligned pores could not only substantially promote water permeation but also enhance the membrane's ability to reject salt. Adding a second NPG layer immediately adjacent to the first ( $H = 3.35$  Å) only reduces the water permeability by 1.5× while increasing the salt rejection from ~75% to >95%. We also find that greater pore offsets can significantly promote salt rejection. However, when the layers are spaced very closely together ( $H < 5.5$  Å), offset pores can completely block water passage. At  $H = 8$  Å, the interlayer space region is sufficiently large to allow water permeation but still small enough to impede salt passage. The second NPG layer reduces the water permeability by 2× in this case, and salt rejection increases for greater pore offsets.

To achieve multilayer NPG membranes with high water permeability and salt rejection, we thus propose several design

guidelines: (1) If both pore alignment and layer separation could be precisely controlled, a multilayer NPG membrane with the smallest possible layer separation and fully aligned pores would represent the most promising choice. Additional layers serve to enhance the membrane's ability to reject salt; (2) If only layer separation can be precisely controlled, it would be preferable to have a sufficiently large layer separation (i.e., 8 Å), in order to avoid fully impeding water passage across misaligned pores. Although large pore offsets would lead to a lower flux (per membrane area), salt rejection could be enhanced. Additional NPG layers could be also used to further increase salt rejection; (3) If only pore offset can be controlled experimentally, our study suggests that a membrane with fully aligned pores is desirable. Although a large layer separation may result in lower salt rejection, more layers could then be superimposed to achieve the requisite salt rejection; (4) If neither pore alignment nor layer separation can be controlled, having an NPG membrane with the greatest possible pore density is recommended in order to enhance the likelihood of having aligned pores. Furthermore, a larger pore density also results in a higher net water flux per area.

Finally, this work provides additional context to compare the relative performance of graphene versus conventional polyamide membranes. A multilayer NPG membrane with the same thickness as a polyamide film (~200 nm) would consist of approximately 200 graphene layers. The permeability of this 200-layer NPG membrane would be approximately 2 L/m<sup>2</sup>·h-bar, which is on the same order of magnitude as the permeability of a typical polyamide film. This implies that the main advantage of NPG relative to polyamide may be its thinness, or more specifically its ability to reject salt within one or a few layers and the possibility of producing NPG in ultrathin sheets. In contrast, in polyamide it is difficult to synthesize films thinner than 100–200 nm, because the film thickness is governed by the mass transfer of the diamine to the organic phase during interfacial polymerization,<sup>35</sup> and it is uncertain at any rate that a significantly thinner polyamide film would exhibit high enough salt rejection. To the extent that multilayer graphene brings NPG membranes closer to commercial feasibility and remains orders of magnitude thinner than polyamide membranes, this material represents a promising candidate for future water desalination. Overall, this work has highlighted the potential of multilayer NPG as a promising material that retains many of the exceptional properties of monolayer NPG in a form that may offer greater flexibility in experimental synthesis and long-term membrane production.

## ■ ASSOCIATED CONTENT

### ● Supporting Information

The Supporting Information is available free of charge on the ACS Publications website at DOI: [10.1021/acs.nanolett.5b04089](https://doi.org/10.1021/acs.nanolett.5b04089).

Additional figures as described in the text ([PDF](#))

## ■ AUTHOR INFORMATION

### Corresponding Author

\*E-mail: [jcg@mit.edu](mailto:jcg@mit.edu).

### Author Contributions

D.C.-T. and L.-C.L. contributed equally to this work.

### Notes

The authors declare no competing financial interest.

## ACKNOWLEDGMENTS

The research was supported by Lockheed Martin Corporation. This work was supported by NWO Exakte Wetenschappen (Physical Sciences) for the use of supercomputer facilities, with financial support from the Nederlandse Organisatie voor Wetenschappelijk Onderzoek (Netherlands Organization for Scientific Research, NWO). This work also used the Extreme Science and Engineering Discovery Environment (XSEDE), which is supported by National Science Foundation grant number ACI-1053575.

## REFERENCES

- (1) Cohen-Tanugi, D.; McGovern, R. K.; Dave, S. H.; Lienhard, J. H.; Grossman, J. C. *Energy Environ. Sci.* **2014**, *7*, 1134–1141.
- (2) Konatham, D.; Yu, J.; Ho, T. A.; Striolo, A. *Langmuir* **2013**, *29*, 11884–11897.
- (3) Cohen-Tanugi, D.; Grossman, J. C. *Nano Lett.* **2012**, *12*, 3602–3608.
- (4) Cohen-Tanugi, D.; Grossman, J. C. *Nano Lett.* **2014**, *14*, 6171–6178.
- (5) Reina, A.; Jia, X.; Ho, J.; Nezich, D.; Son, H.; Bulovic, V.; Dresselhaus, M. S.; Kong, J. *Nano Lett.* **2009**, *9*, 30–35.
- (6) Grantab, R.; Shenoy, V. B.; Ruoff, R. S. *Science* **2010**, *330*, 946–948.
- (7) O'Hern, S. C.; Stewart, C. A.; Boutilier, M. S. H.; Idrobo, J.-C.; Bhaviripudi, S.; Das, S. K.; Kong, J.; Laoui, T.; Atieh, M.; Karnik, R. *ACS Nano* **2012**, *6*, 10130–10138.
- (8) Li, X.; Magnuson, C. W.; Venugopal, A.; Tromp, R. M.; Hannon, J. B.; Vogel, E. M.; Colombo, L.; Ruoff, R. S. *J. Am. Chem. Soc.* **2011**, *133*, 2816–2819.
- (9) Ko, Y. U.; Cho, S. R.; Choi, K. S.; Park, Y.; Kim, S. T.; Kim, N. H.; Kim, S. Y.; Chang, S. T. *J. Mater. Chem.* **2012**, *22*, 3606–3613.
- (10) Zhang, C.; Tjiu, W. W.; Fan, W.; Huang, S.; Liu, T. *J. Mater. Chem.* **2012**, *22*, 11748–11754.
- (11) Bae, S.-Y.; Jeon, I.-Y.; Yang, J.; Park, N.; Shin, H. S.; Park, S.; Ruoff, R. S.; Dai, L.; Baek, J.-B. *ACS Nano* **2011**, *5*, 4974–4980.
- (12) Wu, X.; Zhao, H.; Murakawa, H. *J. Nanosci. Nanotechnol.* **2014**, *14*, 5697–5702.
- (13) Ye, X.; Huang, T.; Lin, Z.; Zhong, M.; Li, L.; Yan, Y.; Zhu, H. *Carbon* **2013**, *61*, 329–335.
- (14) Zou, R.; Zhang, Z.; Xu, K.; Jiang, L.; Tian, Q.; Sun, Y.; Chen, Z.; Hu, J. *Carbon* **2012**, *50*, 4965–4972.
- (15) Liu, G.; Jin, W.; Xu, N. *Chem. Soc. Rev.* **2015**, *44*, 5016–5030.
- (16) Huang, L.; Zhang, M.; Li, C.; Shi, G. *J. Phys. Chem. Lett.* **2015**, *6*, 2806–2815.
- (17) Xue, M.; Qiu, H.; Guo, W. *Nanotechnology* **2013**, *24*, 505720.
- (18) Kou, J.; Zhou, X.; Lu, H.; Wu, F.; Fan, J. *Nanoscale* **2014**, *6*, 1865–1870.
- (19) Zhu, C.; Li, H.; Zeng, X. C.; Wang, E. G.; Meng, S. *Sci. Rep.* **2013**, *3*, 3163.
- (20) Lin, L.-C.; Choi, J.; Grossman, J. C. *Chem. Commun.* **2015**, *51*, 14921–14924.
- (21) Lin, L.-C.; Grossman, J. C. *Nat. Commun.* **2015**, *6*, 8335.
- (22) Heiranian, M.; Farimani, A. B.; Aluru, N. R. *Nat. Commun.* **2015**, *6*, 8616.
- (23) Frenkel, D.; Smit, B. *Understanding Molecular Simulation: from Algorithms to Applications*; Academic Press, 2002.
- (24) Cicero, G.; Grossman, J. C.; Schwegler, E.; Gygi, F.; Galli, G. J. *Am. Chem. Soc.* **2008**, *130*, 1871–1878.
- (25) Humphrey, W.; Dalke, A.; Schulten, K. *J. Mol. Graphics* **1996**, *14*, 33–38.
- (26) Hanwell, M. D.; Curtis, D. E.; Lonie, D. C.; Vandermeersch, T.; Zurek, E.; Hutchison, G. R. *J. Cheminf.* **2012**, *4*, 17.
- (27) Plimpton, S. *J. Comput. Phys.* **1995**, *117*, 1–19.
- (28) Cohen-Tanugi, D.; Grossman, J. C. *J. Chem. Phys.* **2014**, *141*, 074704.
- (29) Horn, H.; Swope, W. C.; Pitera, J. W.; Madura, J. D.; Dick, T. J.; Hura, G. L.; Head-Gordon, T. *J. Chem. Phys.* **2004**, *120*, 9665–9678.
- (30) Joung, I. S.; Cheatham, T. E. *J. Phys. Chem. B* **2008**, *112*, 9020–9041.
- (31) Beu, T. A. *J. Chem. Phys.* **2010**, *132*, 164513.
- (32) Mooney, D. A.; Mueller-Plathe, F.; Kremer, K. *Chem. Phys. Lett.* **1998**, *294*, 135–142.
- (33) Corry, B. *J. Phys. Chem. B* **2008**, *112*, 1427–1434.
- (34) O'Hern, S. C.; Boutilier, M. S. H.; Idrobo, J.-C.; Song, Y.; Kong, J.; Laoui, T.; Atieh, M.; Karnik, R. *Nano Lett.* **2014**, *14*, 1234–1241.
- (35) Xie, W.; Geise, G. M.; Freeman, B. D.; Lee, H.-S.; Byun, G.; McGrath, J. E. *J. Membr. Sci.* **2012**, *403–404*, 152–161.